IEEE Access
Multidisciplinary ⋮ Rapid Review ⋮ Open Access Journal

Received August 2, 2018, accepted September 19, 2018, date of publication October 1, 2018, date of current version October 25, 2018.

Digital Object Identifier 10.1109/ACCESS.2018.2872760

Compressive Sensing Holographic Microwave Random Array Imaging of Dielectric Inclusion

LULU WANG[1], (Member, IEEE), AND MOSTAFA FATEMI[2], (Fellow, IEEE)
[1]School of Instrument Science and Opto-electronics Engineering, Hefei University of Technology, Hefei 230009, China
[2]Department of Physiology and Biophysics, Mayo Clinic and Mayo Foundation, Rochester, MN 55905, USA

Corresponding author: Lulu Wang (luluwang2015@hfut.edu.cn)

This work was supported in part by the National Natural Science Foundation of China under Grant 61701159, in part by the Natural Science Foundation of Anhui Province under Grant 101413246 and Grant JZ2017AKZR0129, in part by the Fundamental Research Funds for the Central Universities under Grant JZ2018HGTB0236, in part by the Programme of Introducing Talents of Discipline to Universities of China under Grant B12019, in part by the Foundation for Oversea Master Project from Ministry of Education, China, under Grant 2160311028, and in part by the Hefei University of Technology under Grant JZ2018HGTB0236.

ABSTRACT Holographic microwave imaging is an innovative method to image biological objects based on their dielectric properties, which has the advantages of high spatial resolution. However, the image reconstruction method is always a critical issue in holographic microwave imaging. This research aims to investigate the feasibility and effectiveness of applying compressive sensing (CS) technique to the holographic microwave imaging for small dielectric object detection. This paper presents a compressive sensing holographic microwave random array imaging (CS-HMRAI) method for imaging of dielectric objects. A numerical system consists of various dielectric models and imaging processing model are developed to evaluate the proposed approach. The split Bregman (SB) and orthogonal matching pursuit (OMP) algorithms are applied to HMRAI for evaluation of small inclusions embedded in dielectric objects. Various experiments are conducted to identify lesions using the proposed CS-HMRAI method and results are compared with HMRAI and HMRAI via OMP methods. Both simulation and experimental results demonstrate that CS-HMRAI via SB can produce high-quality images and detect arbitrarily shaped small inclusions with random sizes and locations by using significantly fewer sensors and scanning times than the HMRAI and CS-HMRAI via OMP approaches. The proposed approach has the potential for further investigation for breast tumor detection in a fast and cost-effective manner.

INDEX TERMS Microwave imaging, holographic microwave imaging, compressive sensing, split Bregman, orthogonal matching pursuit.

I. INTRODUCTION

Breast cancer is the leading cause of cancer death among females in the United States [1]. Although X-ray mammography is the gold standard imaging tool for early breast tumor detection, it has some drawbacks, such as limited sensitivity and specificity, unsafe radiation, not suitable for young women, uncomfortable due to breast compression [2]. Contrast-enhanced digital mammography offers more accuracy diagnostic in dense breasts than mammography, but it is expensive and produces more radiations [3]. These limitations motivate the search for alternative or complementary technologies for early breast cancer detection. Active microwave imaging (MI) has been proposed as an alternative or additional method to the standard mammography for early breast cancer detection [4]–[7]. The active MI exploits the dielectric contrast between healthy tissue and malignant tissue at microwave frequencies. MI is nonionizing and noninvasive modality, which does not require breast compression and uses low radiation power (much lower than a cell phone). More importantly, MI has the potential to improve sensitivity and specificity even it does not offer high-resolution images as provided by X-rays due to the dielectric contrast (greater than 2:1) is much higher than the contrast in radiographic density exploited by X-rays [8].

Over the past two decades, MI-based techniques have been extensively studied for biomedical applications both numerically and experimentally. However, MI-based techniques have not been extensively studied in clinical

environments due to the limited image resolution, and complicated implementation system such as long data collection time is required [9]. To solve these challenges, some investigators have focused on developing high dynamic measurement systems to capture small inclusions, finding solutions to enhance malignant tissues, and employing fewer sensors to reduce data collection time [10].

Compressed sensing (CS) can reconstruct images using much lower sampling rates than the convention Shannon-Nyquist sampling rate, which offers the potential to reconstruct signals and images from small amounts of data [11]. CS-based techniques have been applied in radar imaging to detect buried objects [12]. Ambrosanio and Pascazio [13] successfully applied CS to random sensor array in a vacuum media. Previous studies have demonstrated that image quality could be improved significantly using CS techniques and random sensor arrays [14]. Various CS iterative algorithms have been applied for signal and image reconstruction, including conjugate gradient (CG) [15], orthogonal matching pursuit (OMP) and majorization–minimization [16], [17], and CS sparse representation matrices [18]. Recently, CS has been applied to several biomedical imaging applications such as MRI and CT [19], [20]. More recently, Bevacqua and Scapaticci [21] applied CS in microwave imaging system to detect breast tumors. They used magnetic nanoparticles as a contrast agent to improve the accuracy of tumor detection. The simulation results showed that CS has the potential to become a new tool to improve image resolution and increase accuracy in cancer detection, as well as reduce the data collection time due to much smaller amounts of data is required.

The authors recently developed a holographic microwave imaging (HMI) method for breast lesion detection and brain stroke detection [22], [23]. The method has been evaluated on various simplified dielectric phantoms. Compared with other MI approaches, HMI could map a dielectric object in free-space, which simplified the measurement system. However, HMI method uses the uniform sensor array which requires large signal and image processing, especially for 3D objects. Previous studies have demonstrated that microwave image is highly related to the sensor array configurations, the random sensor array (non-uniform) offers a better image quality than the uniform sensor array [24].

This paper aims to investigate a CS based holographic microwave random array imaging (CS-HMRAI) for rapid diagnosis of inclusions embedded in a dielectric object model. A numerical imaging system, including a CS-HMRAI model and various realistic breast models, is developed to validate the proposed approach. CS iterative algorithms via split Bregman (SB) and OMP are implemented to reconstruct images of the target object. Various simulations and experiments are conducted to study the feasibility of using CS-HMRAI for inclusion detection in a fast and low-cost manner.

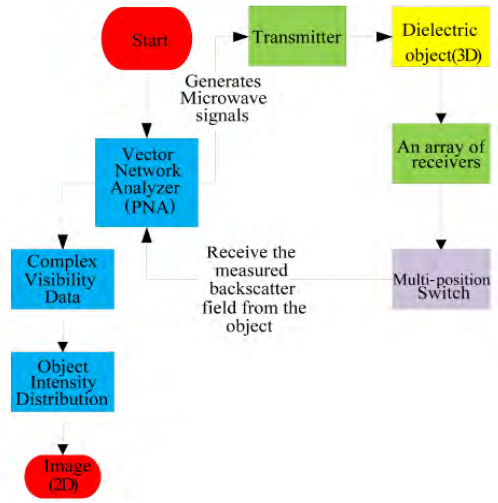

FIGURE 1. HMRAI work process.

II. IMAGE ALGORITHM

A. HOLOGRAPHIC MICROWAVE RANDOM ARRAY IMAGING

Figure 1 shows the working principle of HMRAI system. The system consists of a microwave signal generator (such as vector network analyzer, VNA), an N-element random sensor array (N≥3), a signal control and data acquisition unit, and a computer with the matched program. The random sensor array plane is located under the target object in the far field distance with one sensor works as a transmitter, and other sensors work as detectors. During data collection, the VNA generates microwave signals to the object through the transmitter, and each detector measures the scattered electric field from the object. The object image can be reconstructed from the recorded data by using the HMRAI method.

A point Q is embedded in a 3D object model (Figure 2), in far-field condition, the complex visibility can be computed by any two detectors located at $\overrightarrow{r_a}$ and $\overrightarrow{r_b}$ [25]:

$$V\left(\overrightarrow{r_a}, \overrightarrow{r_b}\right) = \langle \overrightarrow{E}_{scat}\left(\overrightarrow{r_a}\right) \cdot \overrightarrow{E}^{*}_{scat}\left(\overrightarrow{r_b}\right)\rangle \tag{1}$$

Where $\langle\rangle$ denotes the time average, $\overrightarrow{E}_{scat}$ and $\overrightarrow{E}^{*}_{scat}$ denote the scattered field and the conjugate complex of the scattered field, respectively. $\overrightarrow{r_a}$ and $\overrightarrow{r_b}$ are the distance vector from the model to the detectors located at $\overrightarrow{r_a}$ and $\overrightarrow{r_b}$, respectively.

For N detectors, the total complex visibility is:

$$\Upsilon = \sum_{i}^{N} \mathrm{V}\left(\overrightarrow{r_a}, \overrightarrow{r_b}\right), \quad i = 1, \ldots, N;\ N \geq 3,\ \mathrm{a} \neq \mathrm{b} \tag{2}$$

Define the object intensity as [22]:

$$I\left(\overrightarrow{s}\right) = \left(\frac{k_0^2}{4\pi}\right)^2 \left|\varepsilon_r(\overrightarrow{s}) - \varepsilon_0\right|^2 \overrightarrow{E_T}\left(\overrightarrow{s}\right) \cdot \overrightarrow{E_T^*}\left(\overrightarrow{s}\right) \tag{3}$$

Where k_0 is the wavenumber of free-space, ε_r is the relative permittivity of the object, ε_0 is the relative permittivity of free-space, and the total electric field $\overrightarrow{E_T} = \overrightarrow{E}_{inc} + \overrightarrow{E}_{scat}$.

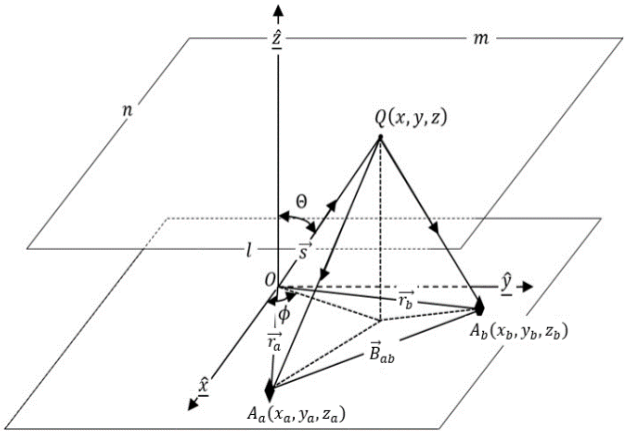

FIGURE 2. Measurement setup of two detectors.

If all sensors located on the same sensor array plane (2D), then the visibility equation can be represented by [23]:

$$V(u_{ab}, v_{ab}) = \iint \tilde{I}_{ij}(l,m) e^{j2\pi(u_{ab}l + v_{ab}m)} dldm \tag{4}$$

Where $\tilde{I}(l,m) = \int_s \frac{I(s,l,m)}{\sqrt{1-l^2-m^2}} ds$, $l = sin\theta cos\phi$, $m = sin\theta sin\phi$ (see Figure 2), $u_{ab} = \frac{(\vec{x_b}-\vec{x_a})}{\lambda_0} = \frac{(\vec{x_b}-\vec{x_a})f}{v_0}$, $v_{ab} = \frac{(\vec{y_b}-\vec{y_a})}{\lambda_0} = \frac{(\vec{y_b}-\vec{y_a})f}{v_0}$, f denotes the frequency, λ_0 is the wavelength in free-space.

The UV coverage and baseline are developed to evaluate the sensor array aperture quantitatively. For any two detectors located at $A_a(x_a, y_a, z_a)$ and $A_b(x_b, y_b, z_b)$, the UV coverage and baseline are defined as:

$$(u_{ab}, v_{ab}) = (x_b - x_a, y_b - y_a)/\lambda_0 \tag{5}$$

$$B_{ab} = \sqrt{u_{ab}^2 + v_{ab}^2} \tag{6}$$

Where λ_0 denotes the wavelength of free-space.

An image can be reconstructed using an inverse faster Fourier transform (IFFT):

$$\tilde{I}_{ab}(l,m) = \iint V(u_{ab}, v_{ab}) e^{-j2\pi(u_{ab}l + v_{ab}m)} dudv \tag{7}$$

The scattered electric field measured by the random sensor array can be considered as a sparse data selected from the uniform sensor array ($M \times M$, such as 64×64 antennas, $N \leq M$). Therefore, the HMRAI image can be reconstructed by:

$$\tilde{I} = \sum_{a,b}^{M} \tilde{I}_{ab}(l,m) = \mathcal{F}_{FFT}^{*}[\Upsilon e^{-j2\pi(u_{ab}l + v_{ab}m)}] \tag{8}$$

Where $\mathcal{F}_{FFT}^{*}$ denotes the inverse fast Fourier transform (IFFT).

B. COMPRESSED SENSING HOLOGRAPHIC MICROWAVE RANDOM ARRAY IMAGING

Over the past two decades, various CS algorithms have been developed for signal and image reconstruction [26]–[30].

TABLE 1. CS optimization algorithms.

Algorithm 1: CS-HMRAI via SB

given maximum iterations N, and tolerance ρ.
Initialize $\hat{I} = \boldsymbol{A}^H \boldsymbol{\Upsilon}$, $c = \boldsymbol{\Upsilon}$, $c_x = c_y = c_w = 0$, and $i = 0$.
while $\varepsilon = (\|\boldsymbol{A}\hat{I} - \boldsymbol{\Upsilon}\|_{\ell_2}^2 / \|\boldsymbol{\Upsilon}\|_{\ell_2}^2) > \rho$ or $i \leq N$ **do**
$w \leftarrow$SoftThresholding $(\boldsymbol{\Psi}\hat{I} + c_w, (1/2\alpha))$;
$d_x \leftarrow$SoftThresholding $(\mathrm{D}_x\hat{I} + c_x, (1/2\beta))$;
$d_y \leftarrow$SoftThresholding $(\mathrm{D}_y\hat{I} + c_x, (1/2\beta))$;
$c_w \leftarrow c_w + \boldsymbol{\Psi}\hat{I} - w$;
$c_x \leftarrow c_x + \mathrm{D}_x\hat{I} - d_x$;
$c_y \leftarrow c_y + \mathrm{D}_y\hat{I} - d_y$;
$c \leftarrow c + \boldsymbol{\Upsilon} - \mathbf{A}\hat{I}$;
$i \leftarrow i + 1$;
end while

Algorithm 2: CS-HMRAI via OMP

Require:
Spare measurements s;
Sparse domain $\boldsymbol{\Psi}$
HMRAI operator $\boldsymbol{\gamma}$
Stopping criteria t_{max} and TolGrad
Ensure:
Reconstructed image $\tilde{I}$;
Initialization: $\beta_o = s$; $\lambda_0 = 0$; $t = 1$;
$B = \boldsymbol{\Psi}\boldsymbol{\gamma}^{-1}$;
$\Gamma_0 = \{B_j\}_{j=1}^{N_{xy}}$;
while $(t \geq t_{max})$ and $\|I_t\|_2 <$TolGrad **do**
$\Gamma_t = \Gamma_{t-1} \backslash \lambda_{t-1}$;
$\lambda_t = \underset{\lambda_j \in \Gamma_t}{argmax} |< \beta_{t-1}, \lambda_j >|$;
$\hat{I} = \underset{I}{argmax} \|BI - s\|_2$;
$\beta_t = BI - s$;
$t = t + 1$;
end while

Among these methods, the Basis Pursuit (BP) and OMP are widely used for image reconstruction. Previous studies have shown that OMP outperforms BP especially when the off-grid effect is considered [31] and OMP is much less computationally intensive and more accessible to implement than the BP algorithm [32]. As a result, this paper focuses on the SB and OMP algorithms. Table 1 presents the CS algorithms for image reconstruction.

The CS techniques emphasize the consistency between the estimated HMRAI image and the actual gathered$k$-space samples. For HMRAI image, the CS technique can be interpreted as [33]:

$$\begin{aligned} &\min_{\hat{I}} \ \alpha \left\| \boldsymbol{\Psi}\hat{I} \right\|_{\ell_1} + \beta \left\| \hat{I} \right\|_{TV} \\ &subject\ to \ \left\| \boldsymbol{A}\hat{I} - \boldsymbol{\Upsilon} \right\|_{\ell_2}^2 \leq \delta^2 \end{aligned} \tag{9}$$

Where $\hat{I}$ is the estimated HMRAI image, α and β are the weights for the consistency of the ℓ_1-norm and TV-norm, respectively. $\|\cdot\|_{TV}$ denotes the 2D isotropic TV operator,

$\boldsymbol{\Upsilon}$ denotes the under-sampled non-uniform k-space data, $\mathbf{A}$ is the measurement matrix that reflects the acquisition of under-sampled data $\boldsymbol{\Upsilon}$, and $\boldsymbol{\Psi}$ is the sparsifying matrix that transforms the image to a sparse representation. δ denotes the accuracy, which depends on the precision, the measurement noise, and the model error.

The gridding CS technique can be applied to recover HMRAI images from under-sampled non-uniform k-space samples. According to equation (7), the measurement operator $\mathbf{A}$ can be represented as:

$$\boldsymbol{A} = U\{I[\mathcal{F}^*_{FFT}(\cdot)]\} \tag{10}$$

Where U denotes the binary matrix that is applied to select the random locations for random under-sampling and $\mathcal{F}^*_{FFT}$ is the IFFT operator.

The SB algorithm is applied to recover HMRAI images. The constrained problem (9) can be transformed as a sequence of unconstrained problems.

$$\hat{I}_{p+1} = \underset{\hat{I}_k}{argmin}\ \frac{\varpi}{2}\left\|A\hat{I}_p - c_p\right\|^2_{\ell_2} + \alpha\left\|\boldsymbol{\Psi}\hat{I}_p\right\|_{\ell_1} + \beta\left\|\nabla\hat{I}_p\right\|_{\ell_1} \tag{11}$$

$$c_{p+1} = c_p + \boldsymbol{\Upsilon} - A\hat{I}_{p+1} \tag{12}$$

Where p denotes the iteration number, ϖ presents the regularization parameter that determine the trade-off between measurement consistency and sparsity in the $\boldsymbol{A}$ domain and the finite difference domain. ∇ is the discrete 2D isotropic TV operator, and $\left\|\nabla\hat{I}_p\right\|_{\ell_1} = \left\|\hat{I}_p\right\|_{TV}$.

Omitting the subscript p, equation (11) is related to prepare for the splitting of the two ℓ_1-norm terms:

$$\underset{\hat{I},w,d_x,d_y}{min}\ \frac{\varpi}{2}\left\|A\hat{I} - c\right\|^2_{\ell_2} + \alpha\left\|w - \boldsymbol{\Psi}\hat{I} - c_w\right\|^2_{\ell_2} + \|w\|_{\ell_1} + \|\nabla d\|_{\ell_1} + \beta\left\|d_x - \nabla_x\hat{I} - c_x\right\|^2_{\ell_2} + \beta\left\|d_y - \nabla_y\hat{I} - c_y\right\|^2_{\ell_2} \tag{13}$$

Where ∇_x and ∇_y denote the 1D discrete derivative operator in X, Y dimension, respectively. d_x, d_y, c_x, c_y and c_w denote the auxiliary variables. The SoftThresholding operator $(x, t) = \max(0, 1 - t/|x|)\, x$ is used to obtain the optimal values of w, d_x, and d_y.

The optimal $\hat{I}$ of the problem (11) can be reduced to the following formula by fixing w, d_x, d_y [34]:

$$\left(\frac{\varpi}{2}A^HA + \alpha\boldsymbol{\Psi}^H\boldsymbol{\Psi} + \beta\nabla_x^T\nabla_x + \beta\nabla_y^T\nabla_y\right)\hat{I} = \frac{\varpi}{2}A^Hb + \alpha\boldsymbol{\Psi}^H(w - b_w) + \beta\nabla_x^T(d_x - c_x) + \beta\nabla_y^T(d_y - c_y) \tag{14}$$

The above problem (14) can be solved by the nonlinear CG method. The OMP method is also applied for HMRAI image reconstruction to evaluate the CS-HMARI via SB approach.

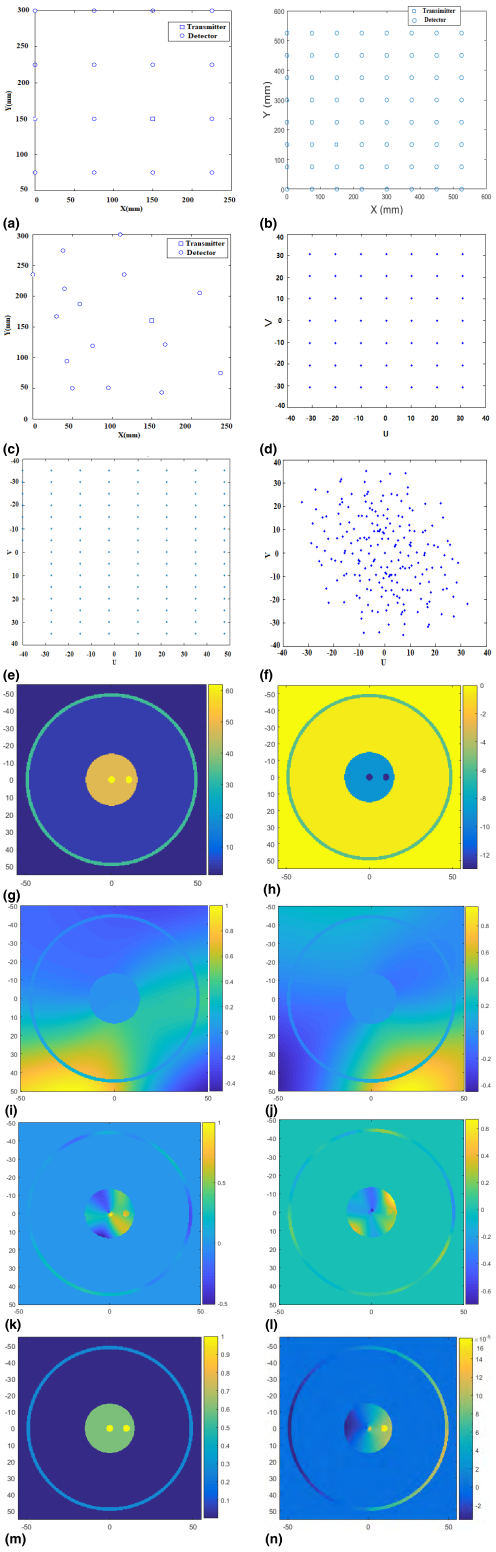

FIGURE 3. (a)-(b) 16-element and 64-element uniform sensor arrays; (c) 16-element random sensor array; (d)-(e) UV coverages of 16-element and 64-element uniform sensor array; (f) UV coverage of random sensor array; Breast model I: (g) Real-part; (h) Imaginary-part; Reconstructed images using 16-element uniform sensor array: (i) Real-part); (j) Imaginary-part; Reconstructed images using 64-element uniform sensor array: (k) Real-part); (l) Imaginary-part; Reconstructed images using random sensor array: (m) Real-part; (n) Imaginary-part.

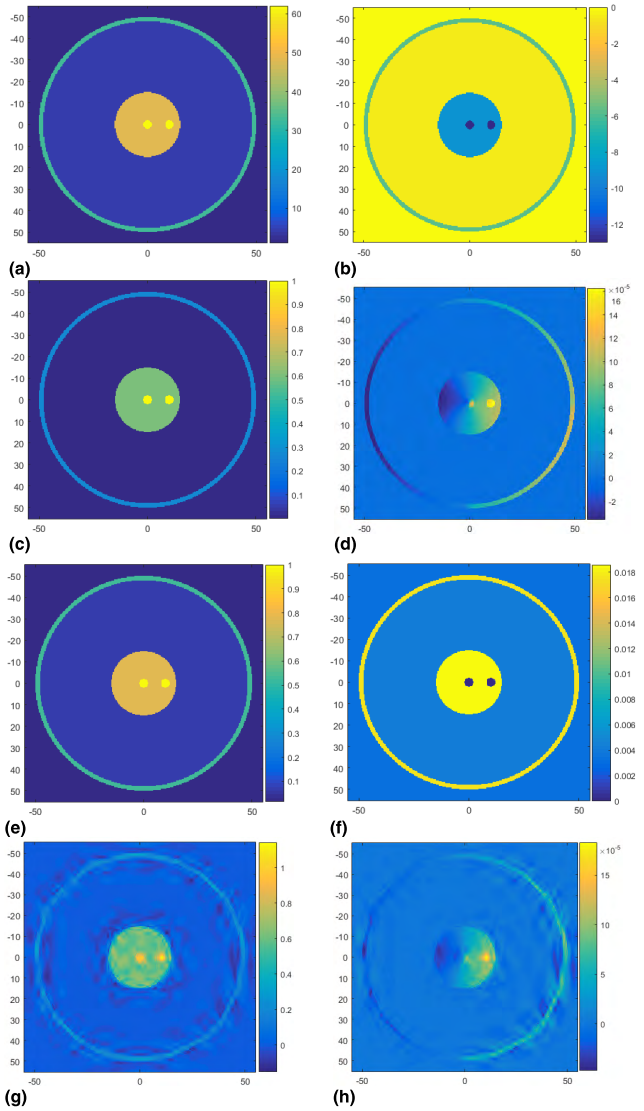

FIGURE 4. Breast model I (noise-free): (a) Real-part; (b) Imaginary-part; Reconstructed images of breast model I using: (c) HMRAI (real-part); (d) HMRAI (imaginary-part); (e) CS-HMRAI via SB (real-part); (f) CS-HMRAI via SB (imaginary-part); (g) CS-HMRAI via OMP (real-part); (h) CS-HMRAI via OMP (imaginary-part).

Besides the visual appearance, the peak signal-to-noise ratio (PSNR) and CPU time are used to quantify the reconstruction performance [35]:

$$PSNR = 10log_{10}(255^2/\sqrt{MSE}) \tag{15}$$

Where $MSE = 1/PQ\sum_{p=1}^{P-1}\sum_{q=1}^{Q-1}[X(p,q) - \hat{X}(p,q)]^2$, (p, q) means pixel location of a $P \times Q$ image, X and $\hat{X}$ are the original image and reconstructed image, respectively. P, Q are the size of the images.

III. NUMERICAL SYSTEM

A numerical system was developed under the MATLAB environment to demonstrate CS-HMRAI approaches for inclusion detection. The system made of a 3D dielectric object model and a 16-element random sensor array. A matching solution medium ($\varepsilon_r = 4$) was filled in the space between the target object and the sensor array [23]. The operation frequency of 10GHz, the total number of 16 antennas, and the distance of 540mm between the sensor array and the object were selected for simulation settings based on previous evaluations [22], [23], [36]. Several simulations were performed to evaluate the CS-HMRAI model. The experiments were performed using MATLAB R2015b on a computer with Intel CPU TM i7-6700 at 3.41GHz and 32GB RAM, and all models were measured in millimeter (mm).

A. FORWARD MODEL

An open-ended rectangular waveguide antenna was modeled as both transmitter and detector. The narrow and broad apertures of the antenna were 7.5mm and 15mm. The transmitter radiates incident electric field:

$$\vec{E}_{inc}\left(\vec{T_{x_m}}\right) = \left(-\frac{jk_0}{2\pi^2}\right)\vec{E}_0\left(\frac{e^{-jk_0\vec{R}_{\vec{T_{x_m}}}}}{\vec{R}_{\vec{T_{x_m}}}}\right) \times A_N B_B h(\theta, \emptyset)\,\vec{P}(\theta, \emptyset) \tag{16}$$

Where $\vec{R}_{\vec{T_{x_m}}}$ denotes the distance vectors from the object to the transmitter located at $\vec{T_{x_m}}$, $\vec{E}_0$ is the wave amplitude of TE10 mode, A_N and B_B are the narrow and board aperture dimensions of the antenna, respectively. $h(\theta, \emptyset)$ is the radiation pattern, and $\vec{P}(\theta, \emptyset)$ is the polarization vector.

B. BACKWARD MODEL

The scattered electric field can be measured by any detector located at $\vec{r_m}$ [37]:

$$\vec{E}_{scat}\left(\vec{r_m}\right) = \left(\frac{k_0^2}{4\pi}\right)\int_V \Delta x_\mu(\vec{s})\{a\vec{E}_T\left(\vec{s}\right) + \left(b\vec{E}_T\left(\vec{s}\right)\cdot\hat{R}_n\right)\hat{R}_n\}G\left(\vec{r_m}, \vec{s}\right)dV \tag{17}$$

Where k_0 denotes the wavenumber of free-space, $\Delta x_\mu(\vec{s}) = \left|\varepsilon_r(\vec{s}) - \varepsilon_0\right|$, ε_r denotes the relative permittivity of the object, ε_0 is the relative permittivity of free-space, and $\vec{E_T} = \vec{E}_{inc} + \vec{E}_{scat}$.

The scattered field was determined by applying Born Approximation [22], and the electric field inside the breast model was modeled approximately as the incident field that exists at the same location but without the object presented in the imaging domain. The scattered electric field can be computed as:

$$\vec{E}_{scat}\left(\vec{r_m}\right) = \left(\frac{k_0^2}{4\pi}\right)\int_V \Delta x_\mu\left(\vec{s}\right)\vec{E}_{inc}\left(\vec{T_{x_m}}, \vec{s}\right) \times G\left(\vec{r_m}, \vec{s}\right)dV = L\Delta x_\mu, \quad i = 3, \cdots, N \tag{18}$$

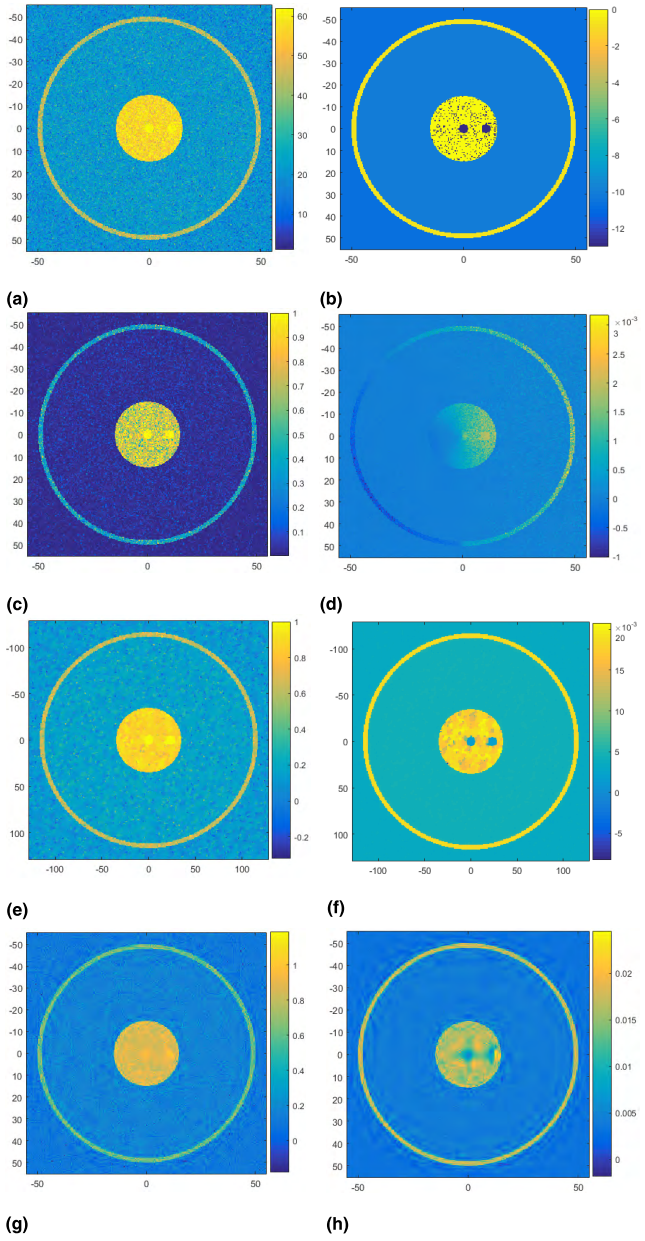

FIGURE 5. Breast model II (contains 10% Gaussian white noise): (a) Real-part; (b) Imaginary-part; Reconstructed images of breast model II using: (c) HMRAI (real-part); (d) HMRAI (imaginary-part); (e) CS-HMRAI via SB (real-part); (f) CS-HMRAI via SB (imaginary-part); (g) CS-HMRAI via OMP (real-part); (h) CS-HMRAI via OMP (imaginary-part).

Where $\left(\overrightarrow{r_i}, \overrightarrow{s}\right) = \nabla g\left(\overrightarrow{r_i}, \overrightarrow{s}\right) \times I, \nabla g\left(\overrightarrow{r_i}, \overrightarrow{s}\right) = \exp\left(-jk_0\left|\overrightarrow{r_i} - \overrightarrow{s}\right|\right)/4\pi\left|\overrightarrow{r_i} - \overrightarrow{s}\right|$, is the scale green function of the medium.

C. BREAST MODEL

Four breast models (TABLE 2) were developed using the published dielectric properties of tissues [38]. The model I ($100 \times 100 \times 50\text{mm}^3$) was made of skin, fat, gland, and two spherical-shaped tumors (4mm in diameter), and it contained $256 \times 256 \times 55$ elements. Breast model II was developed based on Breast model I with 10% white Gaussian noise.

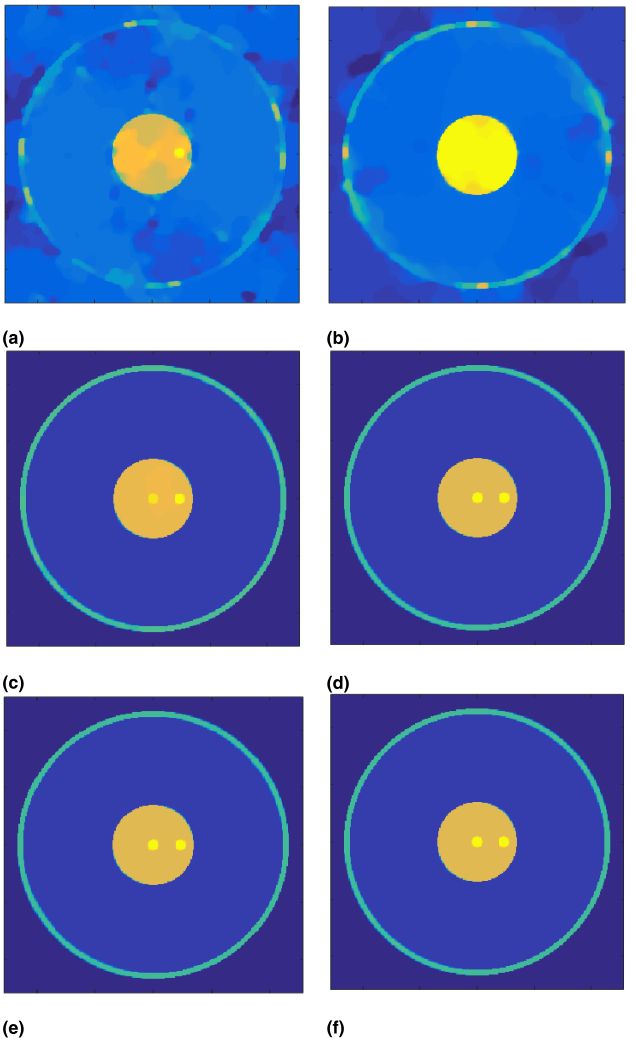

FIGURE 6. Reconstructed images (real-part) of breast model I using CS-HMRAI via SB: (a) 10% measurements; (b) 20% measurements; (c) 30% measurements; (d) 40% measurements; (e) 50% measurements; (f) 60% measurements.

TABLE 2. Location and size of tumors.

Model	Lesion			
	Size (mm)	NO.	Shape	Location (mm)
I	4	2	spherical	$x_1 = 0, y_1 = 0, z_1 = -5$; $x_2 = 10, y_2 = 0, z_2 = -5$;
II	4	2	spherical	$x_1 = 0, y_1 = 0, z_1 = -5$; $x_2 = 10, y_2 = 0, z_2 = -5$;
III	8	1	spherical	random
IV	random	random	random	random

Breast models III and IV were developed based on MRI images. Each model contained 180 images, and each image had 512×512 elements [39]. MATLAB software was used to import MRI images to construct a realistic 3D breast model,

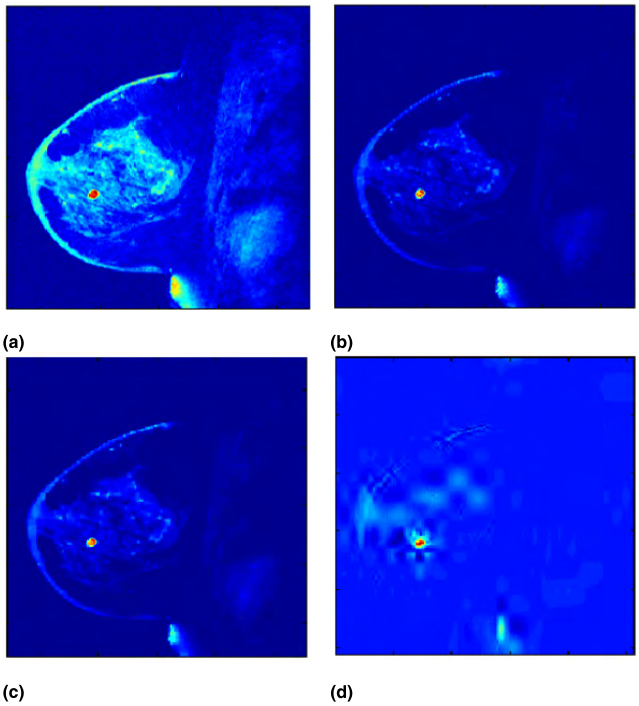

FIGURE 7. (a) Breast model III; reconstructed images using: (b) HMRAI; (c) CS-HMRAI via SB with 30% measurements; (d) CS-HMRAI via OMP with 30% measurements.

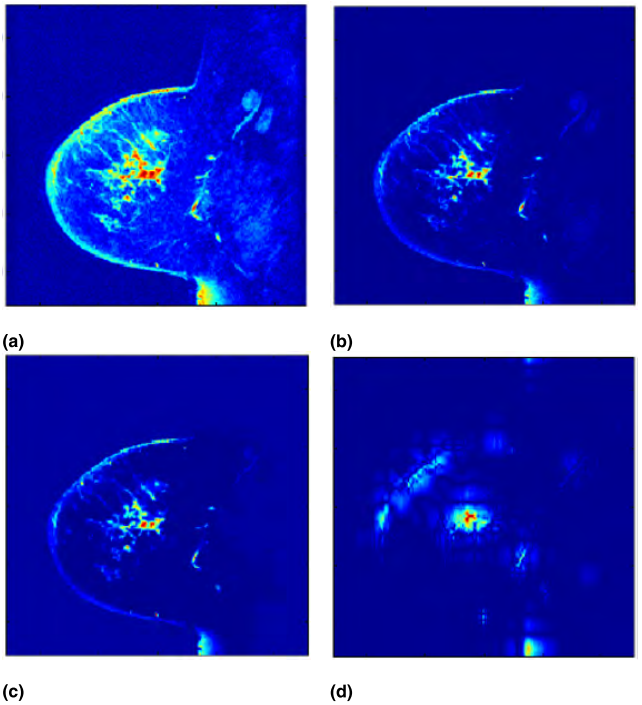

FIGURE 8. (a) Breast model IV includes arbitrarily shaped tumors with random sizes and locations; Reconstructed images using: (b) HMRAI; (c) CS-HMRAI via SB with 30% measurements; (d) CS-HMRAI via OMP with 30% measurements.

and 2D breast models were developed by considering the single slice of MRI-based breast model.

D. NUMERICAL RESULTS

Figures 3(a)-3(f) show the 16-element uniform sensor array, 64-element uniform sensor array, 16-element random sensor array, and their UV coverage performances. Figures 3(g)-3(n) display the original and reconstructed images of breast model I using different sensor arrays. The densities of the three sensor arrays are 0.289, 0.269 and 0.255, respectively. The random sensor array offers a much denser sampling of the UV coverage than the uniform sensor arrays. Inclusions are failed to display in the reconstructed image obtained by using the 16-element uniform sensor array. Both 64-element uniform sensor array and the 16-element random array can detect inclusions embedded in multilayer model. However, the 64-element uniform sensor array used much longer time than the 16-element random sensor array (Table 3, 157.03s vs. 2.72s). The results confirmed that the random array has a potential to produce a high-resolution image in a fast and cost-effective manner due to a smaller number of implementation antennas are required.

Figure 4 displays original and reconstructed images of model I (noise-free) by using HMRAI, CS-HMRAI via SB, and CS-HMRAI via OMP, respectively. Two small inclusions are presented in images obtained by using CS-HMRAI and CS-HMRAI via SB methods.

Figure 5 shows the model II (includes 10% Gaussian noise) and reconstructed images obtained by using HMRAI, CS-HMRAI via SB, and CS-HMRAI via OMP, respectively. CS-HMRAI via SB can fully recover the breast model and identify two tumors successfully.

Figure 6 demonstrates original and the reconstructed images of the model I using CS-HMRAI via SB with different measurements (sampling rates). Two small inclusions could be identified in images obtained with CS-HMRAI via SB with 30% or more measurements.

Figure 7 presents the reconstructed images of model III using HMRAI, CS-HMRAI via SB with 30% measurements, and CS-HMRAI via OMP with 30% measurements, respectively. Results show that the CS-HMRAI via SB and CS-HMRAI via OMP methods can detect small inclusions with correct size and location information.

Figure 8 shows the original and the reconstructed images of model IV obtained using HMRAI, CS-HMRAI via SB with 30% measurements, CS-HMRAI via SB with 100% measurements, and CS-HMRAI via OMP with 30% measurements. Results show that HMRAI and CS-HMRAI via SB with 30% or more measurements can identify the arbitrarily shaped breast tumors with correct size and location information. Color bars in reconstructed images plot signal energy on a linear scale.

Table 3 compares various methods to reconstruct microwave images, including HMI with the 64-element uniform sensor array, HMRAI with the 16-element non-uniform

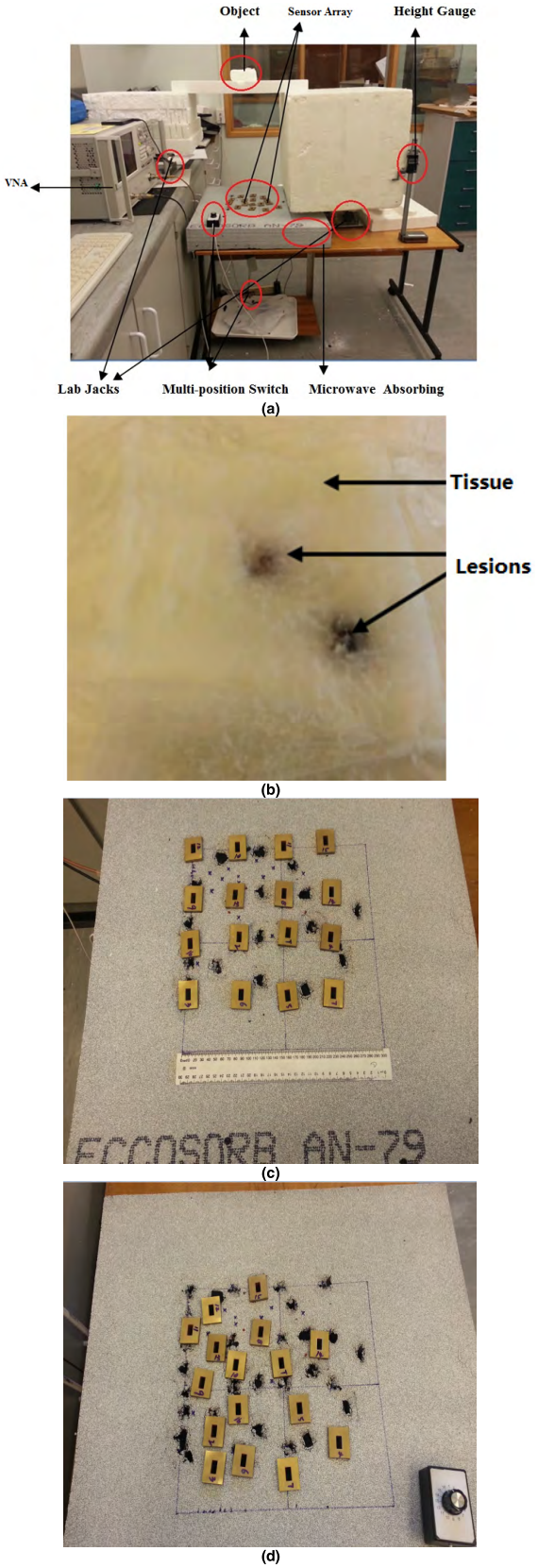

FIGURE 9. (a) Experimental system setup; (b) Phantom under test; (c) 16-element uniform sensor array; (d) 16-element random sensor array.

TABLE 3. Comparison of different imaging methods.

	CS-HMRAI via SB			CS-HMRAI via OMP	HMRAI	HMI
Sampling rate (SR)	10%	30%	50%	30%	100%	100%
PSNR (dB)	25.45	26.67	28.33	24.11	28.32	22.73
Time (s)	2.08	2.09	2.10	5.00	2.72	157.03

sensor array, CS-HMRAI via SB, and CS-HMRAI via OMP. CS-HMRAI via SB offers a better image with a significantly shorter time than HMI, HMRAI, and CS-HMRAI via OMP approaches.

IV. EXPERIMENTAL VALIDATION

The experimental validation was performed to evaluate the proposed method by identifying inclusions embedded in a tissue-like phantom (see Figure 9). The phantom made of emulsifying ointment includes 30% emulsifying wax, 50% soft paraffin and 20% liquid paraffin (to simulate fat tissue), and small grapes (7mm and 15mm in diameter) to simulate lesions [25]. The dielectric properties of emulsifying ointment and grape were close to those of real fat tissue and breast tumor. The Agilent N5230A VNA was connected to antennas that embedded in a microwave absorbing plane, and the sensor array was placed under the phantom in a far field (540mm) with one sensor worked as the transmitter, and other sensors worked as detectors. Two adjustable lab jackets and height gauge were used to adjust the distance between the target and the sensor array. During data collection, the VNA excited microwave signals to the phantom at 10GHz and detectors measured the scattered electric fields from the phantom. Background (without phantom presented) was measured before the data collection. The 2D images were produced using the algorithms detailed above.

Figure 10 shows the reconstructed images of the phantom obtained by using HMI with the 16-element uniform sensor array, HMRAI, CS-HMRAI via SB with 10% measurements, CS-HMRAI via SB with 100% measurements, and CS-HMRAI via OMP methods, respectively. HMI with 16-element uniform sensor array could not identify small inclusions except artifacts. CS-HMRAI via SB could produce good quality images and identify two inclusions with correct size and location information. Some artifacts are displayed in the reconstructed image using CS-HMRAI via SB with 10% measurements and CS-HMRAI via OMP. Color bars in the images plot power density on a linear scale that is normalized to the maximum in the image space.

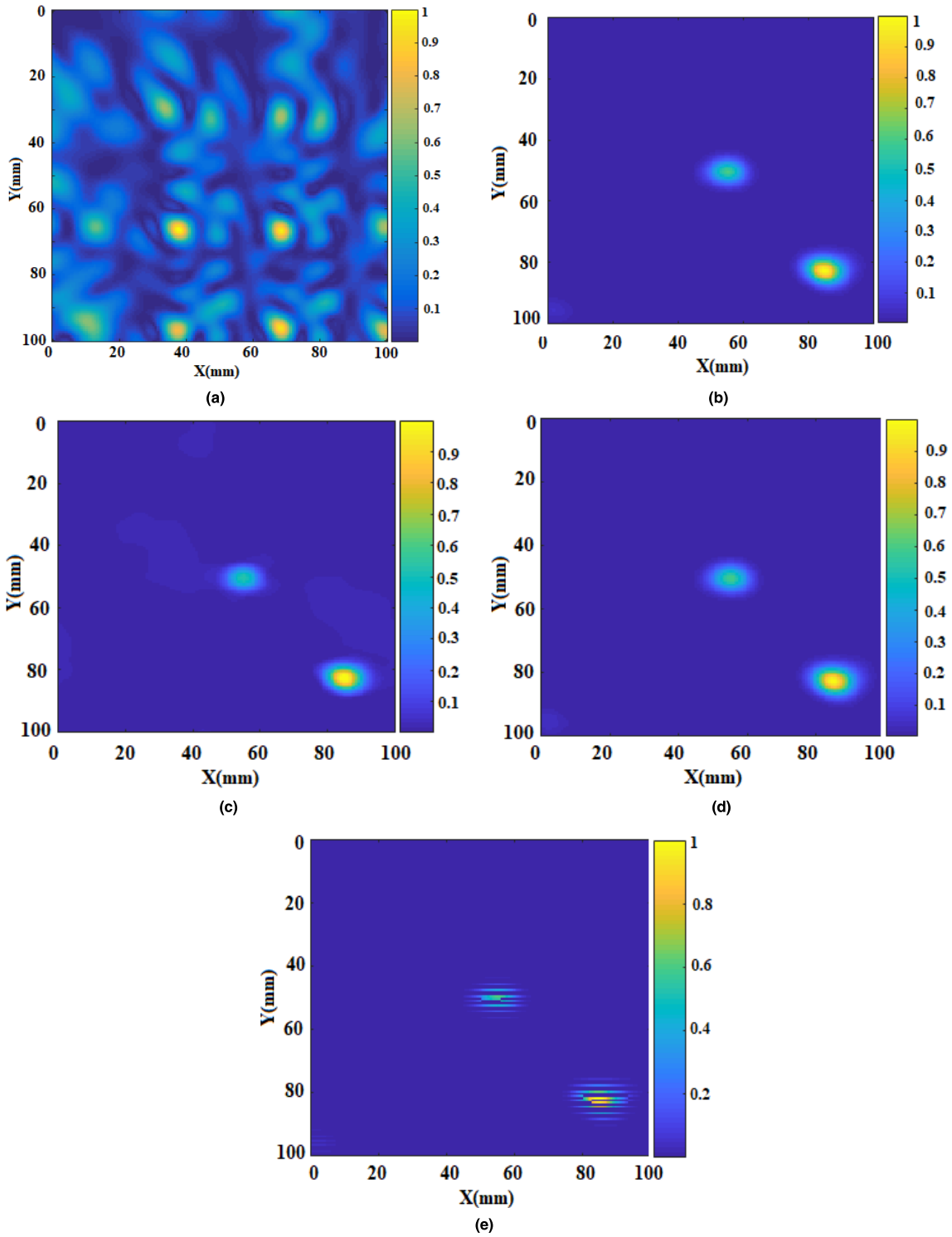

FIGURE 10. Reconstructed images of the phantom using: (a) 16-element uniform sensor array; (b) HMRAI; (c) HMRAI via SB with 10% measurements; (d) HMRAI via SB with 100% measurements; (e) HMRAI via OMP.

V. CONCLUSION

This paper reported the application of CS algorithms in HMRAI method for diagnosis of small dielectric inclusions. The SB and OMP algorithms were implemented to generate CS-HMRAI images. Various simulation and experimental validations were performed to evaluate the proposed approach for dielectric object detection. CS-HMRAI via SB method could fully recover the dielectric object and detect inclusions using much fewer measurements and less data collection time than HMRAI and CS-HMRAI via OMP

approaches. Additionally, CS-HMRAI via SB can produce fewer artifacts than the HMI with the 16-element uniform sensor array, HMRAI and CS-HMRAI via OMP approaches. The obtained results showed that the CS-HMRAI via SB approach could successfully identify small inclusions in a fast and cost-effective manner due to the implementation system requires much fewer antennas, which has the potential to become a useful computer tool for fast visualization and optimization of MI-based techniques.

REFERENCES

[1] *U.S. Breast Cancer Statistics 2017*. Accessed: Oct. 1, 2018. [Online]. Available: https://www.breastcancer.org/symptoms/understand_bc/statistics
[2] M. R. Mohebian, H. R. Marateb, M. Mansourian, M. A. Mañanas, and F. Mokarian, "A hybrid computer-aided-diagnosis system for prediction of breast cancer recurrence (HPBCR) using optimized ensemble learning," *Comput. Struct. Biotechnol. J.*, vol. 15, pp. 75–85, Dec. 2017.
[3] T. Onega *et al.*, "Facility mammography volume in relation to breast cancer screening outcomes," *J. Med. Screening*, vol.23, no. 1, pp. 31–37, 2016.
[4] T. C. Lewis *et al.*, "Contrast-enhanced digital mammography: A single-institution experience of the first 208 cases," *Breast J.*, vol. 23, no. 1, pp. 67–76, 2017.
[5] X. Zhu, Z. Zhao, J. Wang, J. Song, and Q. H. Liu, "Microwave-induced thermal acoustic tomography for breast tumor based on compressive sensing," *IEEE Trans. Biomed. Eng.*, vol. 60, no. 5, pp. 1298–1307, May 2013.
[6] E. Khosrowshahli and A. Jeremić, "Bayesian estimation of tumours in breasts using microwave imaging," *Antimicrob Agents Chemother*, vol. 52, no. 5, pp. 1670–1676, 2013.
[7] M. Klemm, I. Craddock, J. Leendertz, and A. Preece, "Experimental and clinical results of breast cancer detection using UWB microwave radar," in *Proc. IEEE Antennas Propag. Soc. Int. Symp.*, San Diego, CA, USA, Jul. 2008, pp. 1–4.
[8] N. K. Nikolova, "Microwave imaging for breast cancer," *IEEE Microw. Mag.*, vol. 12, no. 7, pp. 78–94, Dec. 2011.
[9] E. Porter, M. Coates, and M. Popović, "An early clinical study of time-domain microwave radar for breast health monitoring," *IEEE Trans. Biomed. Eng.*, vol. 63, no. 3, pp. 530–539, Mar. 2016.
[10] R. Chandra, H. Zhou, I. Balasingham, and R. M. Narayanan, "On the opportunities and challenges in microwave medical sensing and imaging," *IEEE Trans. Biomed. Eng.*, vol. 62, no. 7, pp. 1667–1682, Jul. 2015.
[11] E. Porter, H. Bahrami, A. Santorelli, B. Gosselin, L. A. Rusch, and M. Popović, "A wearable microwave antenna array for time-domain breast tumor screening," *IEEE Trans. Med. Imag.*, vol. 35, no. 6, pp. 1501–1509, Jun. 2016.
[12] E. J. Candès, "Compressive sampling," *Marta Sanz Sol*, vol. 17, no. 2, pp. 1433–1452, 2007.
[13] M. Ambrosanio and V. Pascazio, "A compressive-sensing-based approach for the detection and characterization of buried objects," *IEEE J. Sel. Topics Appl. Earth Observ. Remote Sens.*, vol. 8, no. 7, pp. 3385–3395, Jul. 2015.
[14] L. Carin, "On the relationship between compressive sensing and random sensor arrays," *IEEE Antennas Propag. Mag.*, vol. 51, no. 5, pp. 72–81, Oct. 2009.
[15] C. G. Graff and E. Y. Sidky, "Compressive sensing in medical imaging," *Appl. Opt.*, vol. 54, no. 8, pp. 23–44, 2015.
[16] H. Zhu, Y. Xiao, and S. Y. Wu, "Large sparse signal recovery by conjugate gradient algorithm based on smoothing technique," *Comput. Math. Appl.*, vol. 66, no. 1, pp. 24–32, 2013.
[17] J. Wang, S. Kwon, and B. Shim, "Generalized orthogonal matching pursuit," *IEEE Trans. Signal Process.*, vol. 60, no. 12, pp. 6202–6216, Dec. 2012.
[18] Z. Wang, P. Babu, and D. P. Palomar, "Design of PAR-constrained sequences for MIMO channel estimation via majorization-minimization," *IEEE Trans. Signal Process.*, vol. 64, no. 23, pp. 6132–6144, Dec. 2016.
[19] S. G. Lingala, E. Dibella, and M. Jacob, "Deformation corrected compressed sensing (DC-CS): A novel framework for accelerated dynamic MRI," *IEEE Trans. Med. Imag.*, vol. 34, no. 1, pp. 72–85, Jan. 2015.
[20] M. S. Lee *et al.*, "Compressed-sensing (CS)-based 3D image reconstruction in cone-beam CT (CBCT) for low-dose, high-quality dental X-ray imaging," *J. Korean Phys. Soc.*, vol. 63, no. 5, pp. 1066–1071, 2013.
[21] M. T. Bevacqua and R. A. Scapaticci, "A compressive sensing approach for 3D breast cancer microwave imaging with magnetic nanoparticles as contrast agent," *IEEE Trans. Med. Imag.*, vol. 35, no. 2, pp. 665–673, Feb. 2016.
[22] L. Wang, A. M. Al-Jumaily, and R. Simpkin, "Imaging of 3-D dielectric objects using far-field holographic microwave imaging technique," *Prog. Electromagn. Res. B*, vol. 61, pp. 135–147, Oct. 2014.
[23] L. Wang, A. M. Al-Jumaily, and R. Simpkin, "Holographic microwave imaging for medical applications," *J. Biomed. Sci. Eng.*, vol. 6, no. 8, pp. 823–833, 2013.
[24] L. Wang, A. M. Al-Jumaily, and R. Simpkin, "Investigation of antenna array configurations using far-field holographic microwave imaging technique," *Prog. Electromagn. Res. M*, vol. 42, pp. 1–11, Jun. 2015.
[25] R. Levanda and A. Leshem, "Synthetic aperture radio telescopes," *IEEE Signal Process. Mag.*, vol. 27, no. 1, pp. 14–29, Jan. 2010.
[26] D. L. Donoho, "Compressed sensing," *IEEE Trans. Inf. Theory*, vol. 52, no. 4, pp. 1289–1306, Apr. 2006.
[27] D. S. Smith, J. C. Gore, T. E. Yankeelov, and W. E. Brian, "Real-time compressive sensing MRI reconstruction using GPU computing and split bregman methods," *Int. J. Biomed. Imag.*, vol. 2012, Oct. 2012, Art. no. 864827.
[28] X.-J. Liu, S.-T. Xia, and F.-W. Fu, "Reconstruction guarantee analysis of basis pursuit for binary measurement matrices in compressed sensing," *IEEE Trans. Inf. Theory*, vol. 63, no. 5, pp. 2922–2932, May 2017.
[29] A. Moshtaghpour, L. Jacques, V. Cambareri, K. Degraux, and C. De Vleeschouwer, "Consistent basis pursuit for signal and matrix estimates in quantized compressed sensing," *IEEE Signal Process. Lett.*, vol. 23, no. 1, pp. 25–29, Jan. 2016.
[30] D. Bi, L. Ma, X. Xie, Y. Xie, X. Li, and Y. R. Zheng, "A splitting Bregman-based compressed sensing approach for radial UTE MRI," *IEEE Trans. Appl. Supercond.*, vol. 26, no. 7, Oct. 2016, Art. no. 0606405.
[31] K. Tu, T. M. Duman, M. Stojanovic, and J. G. Proakis, "Multiple-resampling receiver design for OFDM over Doppler-distorted underwater acoustic channels," *IEEE J. Ocean. Eng.*, vol. 38, no. 2, pp. 333–346, Apr. 2013.
[32] C. R. Berger, Z. Wang, J. Huang, and S. Zhou, "Application of compressive sensing to sparse channel estimation," *IEEE Commun. Mag.*, vol. 48, no. 11, pp. 164–174, Nov. 2010.
[33] W. B. Li, S. H. Song, and F. Luo, "Fast image segmentation by convex minimisation and split Bregman method," *Electron. Lett.*, vol. 49, no. 17, pp. 1073–1074, 2013.
[34] L. He and Y. Wang, "Iterative support detection-based split Bregman method for wavelet frame-based image inpainting," *IEEE Trans. Image Process.*, vol. 23, no. 12, pp. 5470–5485, Dec. 2014.
[35] X. Qu, X. Cao, D. Guo, C. Hu, and Z. Chen, "Combined sparsifying transforms for compressed sensing MRI," *Electron. Lett.*, vol. 46, no. 2, pp. 121–123, 2010.
[36] L. Wang, "Holographic microwave imaging for lesion detection," Ph.D. dissertation, Fac. Des. Creative Technol., School Eng., Auckland Univ. Technol., Auckland, New Zealand, 2013.
[37] S. Silver, *Microwave Antenna Theory and Design*. London, U.K.: Peter Peregrinus Ltd., 1984.
[38] Italian National Research Council. *An Internet Resource for the Calculation of the Dielectric Properties of Body Tissues in the Frequency Range 10 Hz_100 GHz*. Accessed: Oct. 1, 2018. [Online]. Available: http://niremf.ifac.cnr.it/tissprop/
[39] *Cancer Imaging Archive*. Accessed: Oct. 1, 2018. [Online]. Available: https://public.cancerimagingarchive.net/ncia/login.jsf

LULU WANG (M'15) received the Ph.D. and M.E. degrees (Hons.) from the Auckland University of Technology, New Zealand, and the B.E. degree (Hons.) from the Manukau Institute of Technology, New Zealand. She is currently an Associate Professor with the School of Instrument Science and Opto-electronics Engineering, Hefei University of Technology, China. She is the First Author of over 50 peer-reviewed international papers, a ASME book, four book chapters, and five patents on electromagnetic imaging in biomedical applications. Her current research focuses on electromagnetic theory and imaging, respiratory diseases detection technologies, and medical devices. He is a member of several professional societies, including ASME, AAAS, PSNZ, and IPNZ.

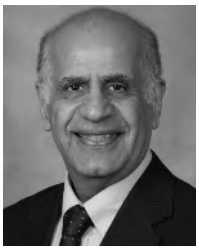

MOSTAFA FATEMI is currently a Professor with the Department of Physiology and Biophysics, Mayo Clinic and Mayo Foundation, Rochester, MN, USA. He and his colleagues provide novel ultrasound-based technologies to investigate mechanical properties of biological tissues. They have developed ultrasound techniques to quantify and image linear and nonlinear elasticity and viscoelastic parameters of tissues. They are also developing new biomarkers based on a novel technique for imaging microvasculature in vivo. He holds over 11 issued patents and many other patent-pending invention disclosures. His research had ongoing support since 1998 by competitive grants from the National Cancer Institute, National Institute of Biomedical Imaging and Bioengineering, National Institute of Diabetes and Digestive and Kidney Diseases, National Science Foundation, Department of Defense Breast Cancer Research Program, Minnesota Partnership for Biotechnology and Medical Genomics, and Susan G. Komen. He upholds team science research and collaborates with scientists, clinicians, and clinical investigators at Mayo Clinic and other academic institutions. He also works with industrial partners to transfer his research to clinical practice.